# Lateral superresolution using *a posteriori* phase shift estimation for a moving object: experimental results

**Sapna A. Shroff,[1,2,3,*] James R. Fienup,[2,3,1] and David R. Williams[2,3]**

[1]*Electrical and Computer Engineering, University of Rochester, Rochester, New York 14627, USA*
[2]*Institute of Optics, University of Rochester, Rochester, New York 14627, USA*
[3]*Center for Visual Science, University of Rochester, Rochester, New York 14627, USA*
[*]*Corresponding author: sapna.shroff@gmail.com*

Received January 29, 2010; revised June 8, 2010; accepted June 9, 2010;
posted June 10, 2010 (Doc. ID 123547); published July 9, 2010

Structured illumination imaging uses multiple images of an object having different phase shifts in the sinusoidally patterned illumination to obtain lateral superresolution in stationary specimens in microscopy. In our recent work we have discussed a method to estimate these phase shifts *a posteriori*, allowing us to apply this technique to non-stationary objects such as *in vivo* tissue. Here we show experimental verification of our earlier simulations for phase shift estimation *a posteriori*. We estimated phase shifts in fluorescence microscopy images for an object having unknown, random translational motion and used them to obtain an artifact-free reconstruction having the expected superresolution. © 2010 Optical Society of America

*OCIS codes:* 100.3020, 100.6640, 050.5080, 170.0180, 070.0070, 110.4850.

## 1. INTRODUCTION

The resolution of an imaging system is limited by the imaging wavelength and numerical aperture. Structured illumination imaging is a technique that has been applied to obtain lateral superresolution in microscopy [1–5]. Other variations and applications of structured illumination have been discussed in several related publications [6–16]. When a sinusoidal illumination is projected on an object, the high-frequency components of the object in the Fourier domain are aliased and shifted into the passband of the imaging system. In order to de-alias and separate these superresolution frequencies from the conventionally accessible frequencies in the image, three or more such sinusoidally patterned images are taken with the phase of the sinusoidal illumination shifted by distinct amounts in each image; a system of equations is then solved to yield the separated components, which are shifted to their appropriate locations and combined. If illumination with a sinusoidal fringe pattern only in one direction is used, it allows superresolution only along the direction perpendicular to the fringes in the sinusoidal illumination. So the processing is repeated for images taken with sinusoidal illumination in different orientations to obtain superresolution in all directions.

Precise and accurate knowledge of the phase shifts in the sinusoidal illumination is necessary for further processing of the images to obtain a superresolved image. Therefore, most prior work has been restricted to stationary objects on anti-vibration stages used with expensive and precise, pre-calibrated translation stages to introduce the phase shifts. We are interested in extending the application of this technique to moving, non-stationary objects such as living, *in vivo* tissue or objects in vibrating environments. We are particularly interested in applying this technique to image the moving human retina *in vivo*. Therefore, we have developed a technique to estimate these phase shifts *a posteriori* and obtain superresolution for a non-stationary object [17–20]. Here we provide experimental verification of our theory by demonstrating its application to a test object having unknown, random translational motion.

## 2. SUPERRESOLUTION WITH SINUSOIDAL ILLUMINATION

We summarize here the concept of superresolution obtained from imaging using a sinusoidal illumination.

### A. Formation of Sinusoidally Patterned Image

Consider a sinusoidal illumination field, $U_{s,n}(x,y) = \cos(2\pi f_o x + \varphi_n)$, which has a spatial frequency of $(f_o, 0)$ and a phase shift of $\varphi_n$. The intensity of this sinusoidal illumination is given by

$$I_{s,n}(x,y) = \frac{1}{2}[1 + m\cos(4\pi f_o x + 2\varphi_n)], \tag{1}$$

which has a spatial frequency of $(2f_o, 0)$ and a phase shift of $2\varphi_n$. The modulation contrast, $m$, is assumed to be 1 for most of our analysis. Let $\mathcal{G}_o$ be the Fourier transform of the intensity of the object and $\mathcal{H}_1$ and $\mathcal{H}_2$ be the optical transfer functions (OTFs) of the illumination and imaging paths, respectively, of the system. Adding noise, $N_n$, to $\mathcal{G}_n$, the Fourier transform of such a sinusoidally patterned image, the effective noisy image in the Fourier domain, as visualized in Fig. 1, is given by [17,18,4]

 

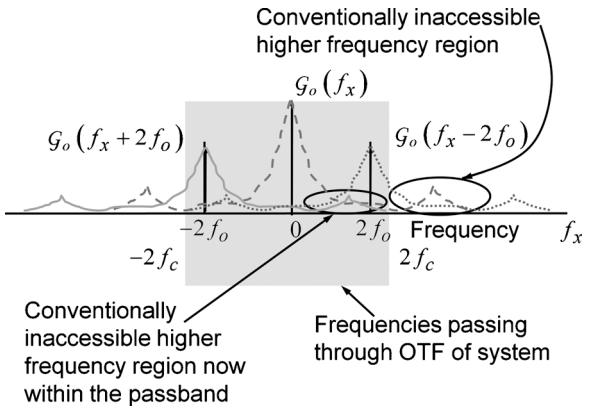


Fig. 1. Visualization of sinusoidal grid patterned image in the Fourier domain [17].

$$\begin{aligned}\hat{\mathcal{G}}_n(f_x,f_y) &= \mathcal{G}_n(f_x,f_y) + N_n(f_x,f_y)\\ &= \frac{1}{2}\mathcal{H}_1(0,0)\mathcal{H}_2(f_x,f_y)\mathcal{G}_o(f_x,f_y)\\ &\quad + \frac{m}{4}\mathcal{H}_1(2f_o,0)e^{i2\varphi_n}\mathcal{H}_2(f_x,f_y)\mathcal{G}_o(f_x-2f_o,f_y)\\ &\quad + \frac{m}{4}\mathcal{H}_1(-2f_o,0)e^{-i2\varphi_n}\mathcal{H}_2(f_x,f_y)\mathcal{G}_o(f_x+2f_o,f_y)\\ &\quad + N_n(f_x,f_y).\end{aligned} \tag{2}$$

If we ignore noise for the moment and assume $N_n(f_x,f_y)=0$, then Eq. (2) consists of three terms each containing copies of the object's Fourier transform: $\mathcal{G}_o(f_x,f_y)$, $\mathcal{G}_o(f_x-2f_o,f_y)$ and $\mathcal{G}_o(f_x+2f_o,f_y)$. The term $\mathcal{G}_o(f_x,f_y)$ is the same as the object information present in a conventional image taken with uniform illumination. But the two copies, $\mathcal{G}_o(f_x-2f_o,f_y)$ and $\mathcal{G}_o(f_x+2f_o,f_y)$, replicate the object's Fourier transform, translated by the spatial frequency of the sinusoidal illumination. These copies effectively drag those portions of the object's Fourier transform, which usually lie outside the passband of the system and are inaccessible in a conventional image, into the passband of the system. Therefore they are treated as the "superresolution" components of our image.

### B. Separation of Overlapping Superresolution and Conventional Components

It is important to separate these overlapping terms from this image in order to utilize the value of this superresolution information. If they are treated as three unknowns, three or more equations would be needed to solve for them. Therefore we take $N$ such sinusoidally illuminated images of the same object, where $N \geqslant 3$, and where the phase of the sinusoidal illumination is shifted by distinct amounts, $2\varphi_n$, where $n=1,2,\ldots N$. Now this system of $N$ images is treated as a linear system of $N$ equations, $AX=B$, where

$$A = \begin{bmatrix} 1 & e^{i2\varphi_1} & e^{-i2\varphi_1} \\ 1 & e^{i2\varphi_2} & e^{-i2\varphi_2} \\ . & . & . \\ . & . & . \\ 1 & e^{i2\varphi_N} & e^{-i2\varphi_N} \end{bmatrix}_{N\times 3}, \tag{3}$$

$$X = \begin{bmatrix} \frac{1}{2}\mathcal{H}_1(0,0)\mathcal{H}_2(f_x,f_y)\mathcal{G}_o(f_x,f_y) \\ \frac{1}{4}m\mathcal{H}_1(2f_o,0)\mathcal{H}_2(f_x,f_y)\mathcal{G}_o(f_x-2f_o,f_y) \\ \frac{1}{4}m\mathcal{H}_1(-2f_o,0)\mathcal{H}_2(f_x,f_y)\mathcal{G}_o(f_x+2f_o,f_y) \end{bmatrix}_{3\times 1}, \tag{4}$$

$$B = \begin{bmatrix} \hat{\mathcal{G}}_1(f_x,f_y) \\ \hat{\mathcal{G}}_2(f_x,f_y) \\ . \\ . \\ \hat{\mathcal{G}}_N(f_x,f_y) \end{bmatrix}_{N\times 1}. \tag{5}$$

This form is improved over that we proposed in [17] in order to track the signal-to-noise ratio (SNR). We solve for vector $X$ by inverting matrix $A$ using singular value decomposition and pseudoinverse [21] and premultiplying it to matrix $B$ as $X=A^{-1}B$. If there were noise in the image, the singular value decomposition and pseudoinverse are reasonably robust at handling noise. The separated components of vector $X$ may be used to obtain a superresolved image. The first term

$$I_{c1}(f_x,f_y) = \frac{1}{2}\mathcal{H}_1(0,0)\mathcal{H}_2(f_x,f_y)\mathcal{G}_o(f_x,f_y), \tag{6}$$

contains the conventional unshifted object component. Correspondingly the OTF affecting this component is given by

$$otf_1(f_x,f_y) = \frac{1}{2}\mathcal{H}_1(0,0)\mathcal{H}_2(f_x,f_y). \tag{7}$$

The terms $\mathcal{H}_1$ and $\mathcal{H}_2$ may be estimated by characterizing the illumination and imaging paths of the system. In our results we assume that we have an aberration-free system and that $\mathcal{H}_1=\mathcal{H}_2$. The second and third terms in vector $X$, containing the superresolution information, are sub-pixel shifted in Fourier space to their appropriate locations to obtain the two superresolution image components,

$$I_{c2}(f_x,f_y) = \frac{1}{4}m\mathcal{H}_1(2f_o,0)\mathcal{H}_2(f_x+2f_o,f_y)\mathcal{G}_o(f_x,f_y) \tag{8}$$

and

$$I_{c3}(f_x,f_y) = \frac{1}{4} m\mathcal{H}_1(-2f_o,0)\mathcal{H}_2(f_x - 2f_o,f_y)\mathcal{G}_o(f_x,f_y), \quad (9)$$

keeping the two terms separate rather than combined as in [18]. The OTF for $I_{c2}$ is given by

$$otf_2(f_x,f_y) = \frac{1}{4} m\mathcal{H}_1(2f_o,0)\mathcal{H}_2(f_x + 2f_o,f_y), \quad (10)$$

and the OTF, $otf_3$, for $I_{c3}$ can be obtained by replacing $2f_o$ in Eq. (10) by $-2f_o$.

These superresolution components extend the passband of the image in the Fourier domain in the direction perpendicular to the fringes in the sinusoidal illumination. In order to obtain superresolution in all directions in Fourier space, this process is repeated with the sinusoidal illumination rotated by, say, 60° and 120°. This gives us similar conventional image components, $I_{c4}$ and $I_{c7}$, having effective OTFs given by $otf_4$ and $otf_7$, and superresolution components, $I_{c5}$, $I_{c6}$, $I_{c8}$, and $I_{c9}$, having effective OTFs given by $otf_5$, $otf_6$, $otf_8$, and $otf_9$, respectively, for the 60° and 120° rotated sinusoidal illumination.

Usually three orientations of the sinusoidal illumination at 0°, 60°, and 120° cover most of the desired extended passband in the frequency domain. However, for lower values of superresolution, such as 50% and less, as depicted in Fig. 2, just two rotations 90° apart are enough to cover most of the extent of the desired extended passband, leaving only modest missing gaps (shown as dark shaded areas in Fig. 2). In the case of two rotations, we have six rather than nine image components. Before we proceed with the combination of these component images, we analyze their SNR.

### C. SNR Analysis

Several factors affect the SNR of the component images. We have performed a similar SNR analysis in [18] and discussed several of these factors. Here we briefly discuss those and also further elaborate on the effect of randomness in phase shifts of the sinusoidal illumination. We consider the particular case of 4 sinusoidally patterned images, where the phase shifts in the sinusoidal illumination are given by $2\varphi_n = 0$, $\pi/2$, $\pi$, and $3\pi/2$, and $\exp(\pm i2\varphi_n) = 1, \pm i, -1$, and $\mp i$. In Appendix A, Eq. (A4), we derive the power SNR for the noisy version of the conventional component image, $\hat{I}_{c1}$, as

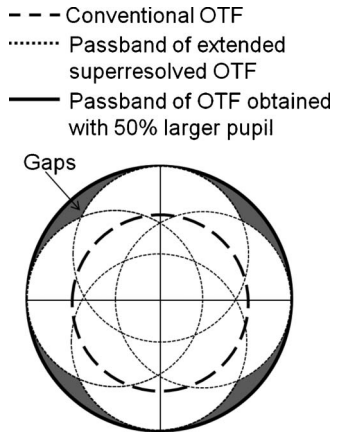


Fig. 2. Visualization of extension of OTF passband with structured illumination.

$$SNR_{c1} = \frac{1}{\sigma^2}|\mathcal{H}_1(0,0)\mathcal{H}_2(f_x,f_y)|^2\Phi_o(f_x,f_y), \quad (11)$$

where $\Phi_o = \langle|\mathcal{G}_o(f_x,f_y)|^2\rangle$ is the object power spectrum and we assume statistically independent noise with variance, $\sigma^2$, in the four sinusoidally patterned images.

The SNR for the noisy version of the superresolution component $\hat{I}_{c2}$ derived in Eq. (A9) in Appendix A is

$$SNR_{c2} = \frac{1}{4\sigma^2}|m\mathcal{H}_1(2f_o,0)\mathcal{H}_2(f_x + 2f_o,f_y)|^2\Phi_o(f_x,f_y). \quad (12)$$

The SNR for $\hat{I}_{c3}$ is similar.

The amount of superresolution increases proportional to the spatial frequency, $2f_o$, of the sinusoidal fringe illumination. From Eqs. (11) and (12) we see that the SNR decreases as $2f_o$ increases, since $\mathcal{H}_1$ decreases with increasing spatial frequency and approaches zero as $2f_o$ approaches the cutoff frequency of the OTF. Hence one should not expect a full 100% superresolution for this case of incoherently imaging a grating onto the object. The illumination and imaging OTFs, $\mathcal{H}_1$ and $\mathcal{H}_2$, and the modulation contrast, $m$, strongly influence the SNR for the superresolution components and can reduce the signal in the superresolution components significantly compared to that in the conventional component images.

The SNR is also affected by the number of sinusoidally patterned images processed to obtain each component image. If $\hat{I}_{c1}$ is obtained by combining $N$ images, then

$$SNR_{c1}(f_x,f_y) = [N/(4\sigma^2)]|\mathcal{H}_1(0,0)\mathcal{H}_2(f_x,f_y)|^2\Phi_o(f_x,f_y). \quad (13)$$

For $N=4$ we obtain the SNR given by Eq. (11), and a greater number of images improves the SNR of the reconstructed image.

In addition, the randomness in the phase shifts in the sinusoidal illumination affects the signal strength in $SNR_{ci}$. To illustrate this effect, consider four images having phase shifts that are not well spaced in the 360° phase space: $2\varphi_n = 0$, $\pi/4$, $\pi/2$, and $3\pi/4$ (covering only 2 quadrants in phase space, unlike the previous case, which covered all 4 quadrants). For this case, the power SNR for the noisy version of the first (conventional image) component, derived optimally in Eq. (A13) in Appendix A, is 6.8 times lower than the SNR obtained in the previous case of well-spaced phase-shifted images given in Eq. (11). The SNR for the noisy version of the superresolution component $I_{c2}$ for the present case, optimally derived in Eq. (A18) in Appendix A, is 3.9 times less than that from the previous case, Eq. (12), and similarly for $I_{c3}$. For this reason it is advantageous to try to obtain images having well-spaced phase shifts in the sinusoidally patterned images to improve the SNR in the reconstruction. If it is not possible to influence the phase shifts, it is advantageous to take a greater number of images to compensate for possibly clumped phase shifts to improve the SNR in the reconstructed image.

We can write the generalized form for the SNR for the component images as

$$SNR_{ci} = \eta_i |otf_i(f_x,f_y)|^2 \frac{\Phi_o}{\Phi_{Ni}}, \tag{14}$$

where $\eta_i$ is a constant that is influenced by the number of sinusoidally patterned images used, the randomness of the phase shifts in the sinusoidally patterned images, as well as a contribution from the SVD and pseudoinverse. Since we have not yet explored this factor in further detail, we set $\eta_i \sim 1$ in our reconstructions. This factor may be investigated in more depth in future.

### D. Multiframe Image Reconstruction

We use a multiframe weighted Wiener–Helstrom-like filter [22,17,18] to appropriately combine these component images to obtain a reconstructed superresolved image,

$$I_{rec}(x,y) = IFT\left\{\sum_{i=1}^{M}\left[\frac{\hat{I}_{ci}(f_x,f_y)}{otf_i(f_x,f_y)} \times \frac{SNR_{ci}}{c + \sum_{j=1}^{M} SNR_{cj}}\right]\right\}, \tag{15}$$

where $\hat{I}_{ci}$ is the noisy estimate of $I_{ci}$ after singular value decomposition and pseudoinverse, and $c$ is a regularization constant that may be varied subjectively to enhance higher spatial frequencies ($c \leq 1$) or to suppress the effect of colored noise in the image ($c > 1$). $c = 1$ is the minimum mean-squared-error solution [22,23]. The SNR weighting used in this filter is given by Eq. (14). $\Phi_o = \langle |\mathcal{G}_o(f_x,f_y)|^2 \rangle$ is the object power spectrum. The conventional image may be used to estimate $\Phi_o$. We consider that the power spectrum of the conventional image is of the form $|otf|^2 \times \mathcal{A}^2 \rho^{-2\alpha} + \Phi_N$, where $\rho$ is the radial spatial frequency coordinate, $\mathcal{A}$ is a constant, $\alpha$ determines how fast the Fourier transform of the object falls off, and $\Phi_N$ is the power spectrum of noise in the conventional image under consideration, assumed to be white noise independent of spatial frequency. $\Phi_o$ is obtained by fitting a curve of this form to the average value of the power spectrum of the conventional image and finding reasonable values to $\mathcal{A}$, $\alpha$, and $\Phi_N$. More details about such curve fitting and the nature of this curve can be found in [24–27]. We estimated $\Phi_o$ approximately from the average of the conventional image components, $I_{c1}$, $I_{c4}$ and $I_{c7}$, obtained from different orientations of the sinusoidal illumination. $\Phi_{Ni}$, the noise power spectrum, can be estimated approximately as the average in a region in a corner of the power spectrum of each component image, $\hat{I}_{ci}$. This region is chosen to lie outside the OTF passband of the image, so it contains only noise. We discussed the effect of these factors and the SNR for each component image in more detail in [18].

Using Eq. (15) and Eq. (14) the multiframe filter is implemented as

$$I_{rec}(x,y) = IFT\left\{\sum_{i=1}^{M}\left[\frac{\hat{I}_{ci}(f_x,f_y) otf_i^*(f_x,f_y)\, \eta_i \frac{\Phi_o}{\Phi_{Ni}}}{c + \sum_{j=1}^{M} \eta_j |otf_j(f_x,f_y)|^2 \frac{\Phi_o}{\Phi_{Nj}}}\right]\right\}. \tag{16}$$

The processing developed in this section has no restriction on the number of sinusoidally patterned images, number of component images, or randomness of the phase shifts used in the sinusoidal pattern. Thus far we have assumed knowledge of these phase shifts, which is essential for artifact-free processing.

## 3. ESTIMATION OF PHASE-SHIFTS IN SINUSOIDALLY PATTERNED IMAGES

In structured illumination imaging, multiple sinusoidally patterned images are taken with distinct phase shifts. Conventionally, for a stationary object, three images are taken, each having 0°, 120°, and 240° phase shifts in the sinusoidal illumination. For a moving object or a vibrating system, it is not possible to introduce such predefined, calibrated phase shifts. Therefore we consider post-processing techniques to estimate these phase shifts *a posteriori*.

One simple and common technique is to average the image along the direction of the sinusoidal fringe and then try to fit an ideal sinusoid to this averaged one. This approach is reasonable for low-frequency sinusoidal patterns, but as the frequency of the sinusoid increases, its contrast decreases, and the accuracy of the phase shift estimate deteriorates substantially. Non-uniformities and features of the object affect the intensity of the sinusoid and disrupt the accuracy of the phase shift estimate. For sinusoids of any orientation other than exactly horizontal or exactly vertical, the averaging process requires interpolation of the value of the sinusoidal illumination, causing further inaccuracies, especially for high-frequency sinusoids.

Another method is an iterative, optimization-based approach [28], where one begins with some preliminary phase estimates and proceeds with the reconstruction of $X$ using these estimates. Inaccuracies in the phase estimates result in residual peaks of the other terms being incompletely separated. This process must be repeated using new phase shift estimates (nudged randomly) until the residual peaks are minimized. However, this is a fairly time-consuming and somewhat random process and would not work without reasonably accurate preliminary estimates.

We use a Fourier domain technique [19,20,17] to estimate this phase shift in the sinusoidal illumination. We compute the Fourier transform of the sinusoidally patterned image. The value of Eq. (2) at $(2f_o, 0)$, which is the location of a peak arising from the spatial frequency of the sinusoidal illumination, is given as

$$\mathcal{G}_n(2f_o,0) = \frac{1}{2}\mathcal{H}_1(0,0)\mathcal{H}_2(2f_o,0)\mathcal{G}_o(2f_o,0) + e^{i2\varphi_n}\frac{m}{4}\mathcal{H}_1(2f_o,0)\mathcal{H}_2(2f_o,0)\mathcal{G}_o(0,0) + e^{-i2\varphi_n}\frac{m}{4}\mathcal{H}_1(-2f_o,0)\mathcal{H}_2(2f_o,0)\mathcal{G}_o(4f_o,0) + N_n(2f_o,0). \quad (17)$$

The first term, $(1/2)\mathcal{H}_1(0,0)\mathcal{H}_2(2f_o,0)\mathcal{G}_o(2f_o,0)$, is weighted by the object Fourier transform at $(2f_o,0)$, and the third term, $e^{-i2\varphi_n}(m/4)\mathcal{H}_1(-2f_o,0)\mathcal{H}_2(2f_o,0)\mathcal{G}_o(4f_o,0)$, is weighted by the object's Fourier transform at $(4f_o,0)$. For a moderately valued spatial frequency of the sinusoid, where $f_o/f_c$ is neither too close to 0 nor 1, both $\mathcal{G}_o(2f_o,0)$, in the first term, and $\mathcal{G}_o(4f_o,0)$, in the third term, lie at the tapering edge of the Fourier transform of an extended object, making $|\mathcal{G}_g(2f_o,0)| \ll \mathcal{G}_g(0,0)$ and $|\mathcal{G}_g(4f_o,0)| \ll \mathcal{G}_g(0,0)$. The second term, $e^{i2\varphi_n}(m/4)\mathcal{H}_1(2f_o,0)\mathcal{H}_2(2f_o,0)\mathcal{G}_o(0,0)$, consists of the object Fourier transform at the origin, which is the largest value of the Fourier transform of the object. In order to obtain a good superresolved image reconstruction we would want good SNR in the raw images. This would imply that the fourth term, $N_n(2f_o,0)$, is also low. Hence in these conditions the most substantial contribution to this equation comes from the second term, and comparatively the contributions from the first, third, and fourth terms are negligible. The object Fourier transform at the origin also happens to have zero phase. The modulation contrast, $m$, seen in this term also has zero phase. If we consider a well-corrected or aberration-free system, then the OTFs, $\mathcal{H}_1$ and $\mathcal{H}_2$, have zero phase. Therefore the factor $e^{i2\varphi_n}$, which arises from the phase of the sinusoidal illumination, is the only phase component in this term. Therefore, to a close approximation, the phase of the term $\mathcal{G}_n(2f_o,0)$ is the phase of the sinusoidal illumination, allowing us to estimate the phase as

$$2\hat{\varphi}_n = \tan^{-1}\left\{\frac{imag[\mathcal{G}_n(2f_o,0)]}{real[\mathcal{G}_n(2f_o,0)]}\right\}, \quad (18)$$

where the arctangent is calculated in Matlab using the atan2 function in which the resulting phase lies between $-\pi$ and $\pi$. Equation (18) can also be applied to any generalized spatial frequency of sinusoidal illumination $(2f_{ox}, 2f_{oy})$ for a rotated fringe pattern.

For conditions of very high spatial frequency of the sinusoidal illumination, where $f_o/f_c \to 1$, the second term, weighted by $\mathcal{H}_1(2f_o,0)\mathcal{H}_2(2f_o,0) \to 0$, also approaches zero. In this case our assumption, that the second term has the most substantial contribution to Eq. (17) and that the contributions from the first, third, and fourth terms to this equation are comparatively negligible, is no longer valid. Therefore this method of phase shift estimation will not provide accurate results for very high spatial frequencies of sinusoidal illumination.

Also, for conditions of very low spatial frequency of the sinusoidal illumination, where $f_o/f_c \to 0$, our assumptions that $|\mathcal{G}_g(2f_o,0)| \ll \mathcal{G}_g(0,0)$ and $|\mathcal{G}_g(4f_o,0)| \ll \mathcal{G}_g(0,0)$ are no longer true. In that case the first and third term no longer have a negligible contribution to the equation. Hence, our method of phase shift estimation will not provide accurate results for very low spatial frequencies of sinusoidal illumination.

Also, if the object Fourier transform is significantly strong at the spatial frequency of the sinusoidal illumination, then the value of the object Fourier transform at the location of the peak of the sinusoidal illumination in frequency domain might add some non-negligible contribution to the phase and introduce some error in the phase shift estimate. This problem may be corrected by using prior knowledge of the object Fourier transform, such as obtained from a conventional image of the object taken with uniform illumination. The value of the object Fourier transform at the location of the peak of the sinusoidal illumination could be subtracted from the value of the peak in frequency domain of the sinusoidally patterned image being used to obtain the phase-shift estimates. For additional precision, iterative optimization-based techniques as mentioned in [28] may be used with these phase shift estimates as an initial starting point.

Most of the above issues related to conditions for validity of this phase shift estimation technique are dealt with in more depth using simulations in [19,20,17].

## 4. EXPERIMENTAL RESULTS

### A. Data Collection and Processing

We have taken images of a high-resolution USAF bar target as a specimen object on a Zeiss fluorescence microscope. We applied some ink from a fluorescent marker pen to the bar target to make it fluoresce. We used a 0.3 NA, 10× objective and a fluoroscein isothiocyanate (FITC) filter cube (excitation ~470 nm and emission ~520 nm). We introduced an additional stop in the light path to reduce the effective NA of the objective to ~0.067 and the resolution to ~3.9 $\mu$m. Then several groups of bars on the USAF bar target were unresolved and could be used to verify superresolution later in our experiment.

We first took a conventional fluorescence image of the object with uniform illumination, a portion of which is shown in Fig. 3(a). We labeled this figure for bars belonging to groups (7,6) to (8,4) that will be referred to in the following discussion. The Fourier transform of the conventional image is shown in Fig. 4(a). All Fourier transform images shown in this paper have been stretched to display dim details. It can be seen that the finest discernible bars in the conventional image belong to the (7,6) group of the USAF bar target, having a spacing of 228 lp/mm (i.e. 4.4 $\mu$m).

We assumed a perfect, unaberrated system and used a resolution of ~3.7 $\mu$m (the calculated 3.9 $\mu$m with a +5% allowance for possible error in the numerical aperture and wavelength) to obtain an approximate, ideal OTF of the imaging path. We used this OTF to deconvolve the conventional image using a Weiner filter to obtain the image shown in Fig. 3(b) and its Fourier transform in Fig. 4(b). We used fairly aggressive deconvolution, with $c = 0.1$, to ensure that high-frequency information is not missed, at the expense of some colored noise. One could be less aggressive and use a larger value of $c$. This would reduce the colored noise in the reconstruction at the cost of

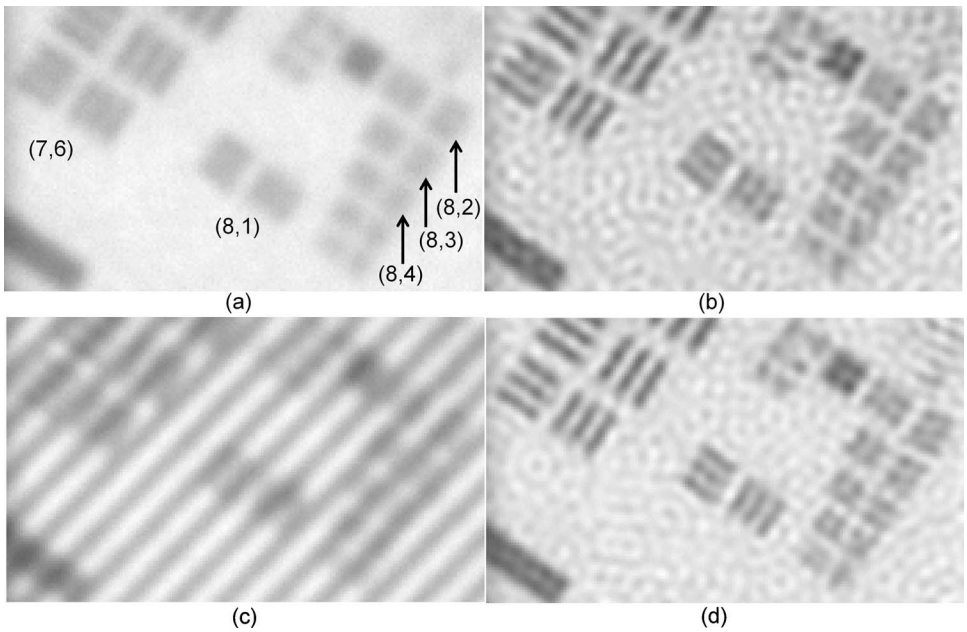


Fig. 3. (a) Conventional image, (b) deconvolved conventional image, (c) sinusoidal grid patterned image, (d) deconvolved noise-reduced conventional image.

slightly poorer resolution. This figure shows that the finest visible bars in the deconvolved conventional image belong to the group (8,1) of the USAF bar target having a spacing of 256 lp/mm (i.e., 3.9 $\mu$m). This implies that the 256 lp/mm bars, lying close to the resolution limit, were probably present in the conventional image, but did not have strong enough contrast to be visible until after the aggressive deconvolution. This verifies that 3.9 $\mu$m is within the resolution limit of our system. Bars with finer spacing than this were still not visible since deconvolution does not increase the resolution of the system, and these spatial frequencies continue to be absent in the deconvolved conventional image. This is also seen in the Fourier domain Fig. 4(b), which does not show any increase in the extent of the Fourier domain of the deconvolved image.

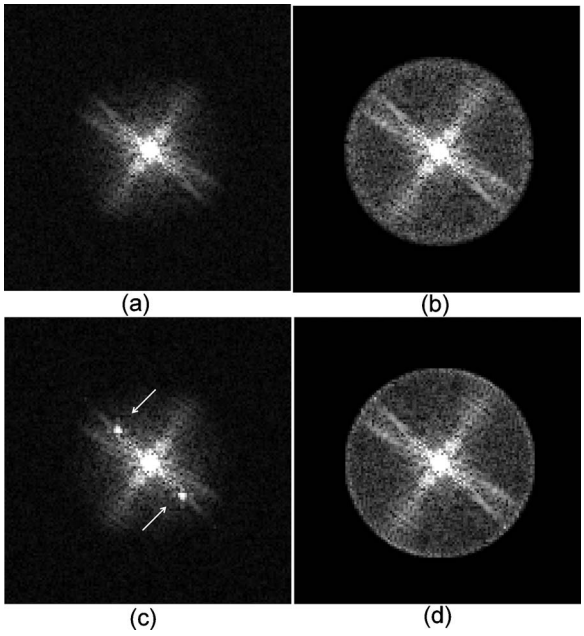


Fig. 4. Stretched Fourier transform of (a) conventional image, (b) deconvolved conventional image, (c) sinusoidal grid patterned image, (d) deconvolved noise-reduced conventional image.

We then inserted in the illumination path a sinusoidal grid having a spatial frequency at ~47% of the cutoff frequency of the imaging system, and we imaged the object with this sinusoidal illumination pattern. One such sinusoidally patterned image is shown in Fig. 3(c) and its Fourier transform in Fig. 4(c), which shows distinct peaks, labeled by white arrows, arising from the spatial frequency of the sinusoidal grid pattern in the illumination. We took a set of 20 such sinusoidally patterned images, where the object was moved in each image by translating the object stage of the microscope by random, unknown amounts.

In our theoretical discussion in Section 2 above, we took three such sets of sinusoidally patterned images with three rotations of the sinusoidal pattern, each spaced 60° apart. Here, we are aiming at only ~47% superresolution, and it was therefore enough to take two sets of grid orientations, rotated 90° apart, to cover most of the Fourier space in the superresolved reconstruction without missing gaps in the extended passband. This holds true for any object, not just for the USAF bar target. So we rotated the grid by 90° and took another set of 20 images in this orientation. We processed each set of images for each orientation separately.

We first used these images to verify the resolution of our system. Using the bars on the USAF bar target as reference, the fringe spacing in the image domain is ~7.8 $\mu$m. From the grid peaks in the Fourier domain, we estimated the grid frequency in the $256\times256$ pixel Fourier transform of each sinusoidally patterned image to be ~20.3 pixels. This implies that the calculated resolution of the system, 3.9 $\mu$m, is ~41 pixels in frequency domain. We obtained another rough estimate of the extent of the

passband of the system by summing 20 sinusoidally patterned images having random phase shifts, thereby boosting the SNR of the summed image. In the Fourier transform of this sum, the diagonal streaks from the object can be seen all the way to about 41 pixels in the Fourier domain. This gives us a lower bound on the cutoff frequency of the system because the high spatial frequencies just before the cutoff of the OTF might be drowned in noise, making them not visible. This verifies that the calculated limit of the system (~41 pixels in the Fourier domain and 3.9 $\mu$m in the image domain) is reasonably accurate.

Further, the finest group (8,1) seen in the deconvolved image, having a spacing of 3.9 $\mu$m, translates to ~40.7 pixels in frequency domain, validating that the 40.7 pixels are within the cutoff of the system. However if the cutoff frequency of the system were as close as the calculated value of 41 pixels, it would require tremendously high SNR for this group of bars to be visible. But they are clearly visible even in the deconvolution of a single image, suggesting that the actual cutoff is slightly greater than 41 pixels.

To further pinpoint the cutoff of the system, we deconvolved the conventional image using different OTFs assuming slightly different cutoff frequencies. If the assumed OTF cutoff is too small, then one risks discarding useful signal at the edge of the passband. If the cutoff is too large, then one might include and enhance noise outside the passband. The correct cutoff frequency gives balanced results for the best resolution and the least noise. In the processing for our experiment, the best visual results were obtained for a cutoff frequency of 43 pixels, about 5% greater than our calculated cutoff frequency of ~41 pixels. This seemed to be within plausible experimental error, so henceforth we assume 43 pixels is the cutoff frequency, which is equivalent to ~3.7 $\mu$m resolution in image space.

Now we proceed with processing each set of these sinusoidally patterned images for superresolution. The conventional image was used as a reference to register, to sub-pixel accuracy [29], each set of sinusoidal grid patterned images where the object was moving. Once registered, the object was aligned in all the sinusoidally patterned images, and the phase of the sinusoidal pattern effectively shifted over the object. This phase shift in each image was estimated using Eq. (18) from the aforementioned peaks in the Fourier domain of the sinusoidally patterned images (arising from the Fourier transform of the sinusoid), which are labeled with white arrows in Fig. 4(c). We used upsampled versions [29,19] of the Fourier transforms of the images in the phase shift estimation to improve its accuracy (with an upsampling factor of 37 used here). These phase shift estimates were used to construct the matrix $A$ using Eq. (3), and the Fourier transforms of the 20 images were used to form $B$ using Eq. (5). These were used to solve for vector $X$ on a pixel-by-pixel basis using $X=A^{-1}B$. This was repeated for the image set where the grid was rotated by 90°. We used the separated terms to obtain all component images, $\hat{I}_{ci}$. The corresponding OTFs, $otf_i$, are obtained by using the ideal OTF in Eqs. (7) and (10).

The two conventional components, obtained from the two sets of data taken with two orientations of the sinusoidal illumination, each contain a great deal of noise reduction due to the effective averaging of all the grid images in the singular value decomposition and pseudoinverse. We used these two conventional component images and averaged them to obtain a further noise-reduced conventional image. This noise-reduced conventional image would make a fairer comparison with the superresolution images that have undergone similar averaging. The noise-reduced conventional image was deconvolved using a Weiner filter with a regularization constant $c=0.1$ to obtain the deconvolved noise-reduced conventional image and its Fourier transform shown in Fig. 3(d) and Fig. 4(d), respectively. The image does show significant reduction in the contrast of colored noise and improvement in SNR, but it shows no greater resolution than the conventional deconvolved image. Here, too, the finest visible bars still belong to the group (8,1) of the USAF bar target having a spacing of 256 lp/mm (i.e., 3.9 $\mu$m). Here also, the Fourier domain does not show any increase in the extent of the recovered Fourier transform.

We also employed the component images, $\hat{I}_{ci}$, and corresponding OTFs, $otf_i$, in Eq. (16), with $c=0.1$, and $\eta_i=1$, to produce a superresolved image. As in the conventional image deconvolution, this value of $c$ improved the contrast and visibility of the bars in our reconstruction, although at a cost of increase in colored noise. This gave us the reconstructed image and its Fourier transform with approximately 47% superresolution shown in Fig. 5(a) and Fig. 6(a), respectively. Here the finest visible set of bars belongs to the group (8,4) of the USAF high-resolution bar target having a line spacing of 362 lp/mm (i.e., 2.8 $\mu$m). This was substantially outside the resolution limits of the deconvolved, noise-reduced, conventional image. The Fourier domain also shows an increase in the extent of its non-zero spatial frequencies. The diagonally oriented streaks in the Fourier domain that are characteristic of the bar target can be seen to extend beyond the extent of the conventional OTF. This image is the experimental verification of superresolution.

When the Fourier transform of this superresolved image is stretched and displayed as in Fig. 6(a), it is possible to see that there are some residual peaks in the Fourier domain, labeled by two white arrows, visible from the remnants of one orientation of the sinusoidal illumination in the Fourier domain of the reconstructed superresolved image. Such residual peaks may arise for several reasons. One possibility is imperfections in the phase shift estimates. This could arise due to the slight overlap of the streaks from the object's Fourier transform with the peaks from the Fourier transform of the sinusoidal grid patterned illumination. The residual peaks could also arise if the illumination in the grid-patterned image was non-uniform or varied between images. Another cause could be that there were several images in the set having similar phase shifts. We plot all the phase shifts in our 20 images for both orientations in Fig. 7. There does not appear to be any significantly unusual difference in the spread in the phase shifts for the images in the two orientations. The figure also contains phase shift estimates obtained later in the experiment for fewer images in each set. We are not yet certain as to the exact reason for this

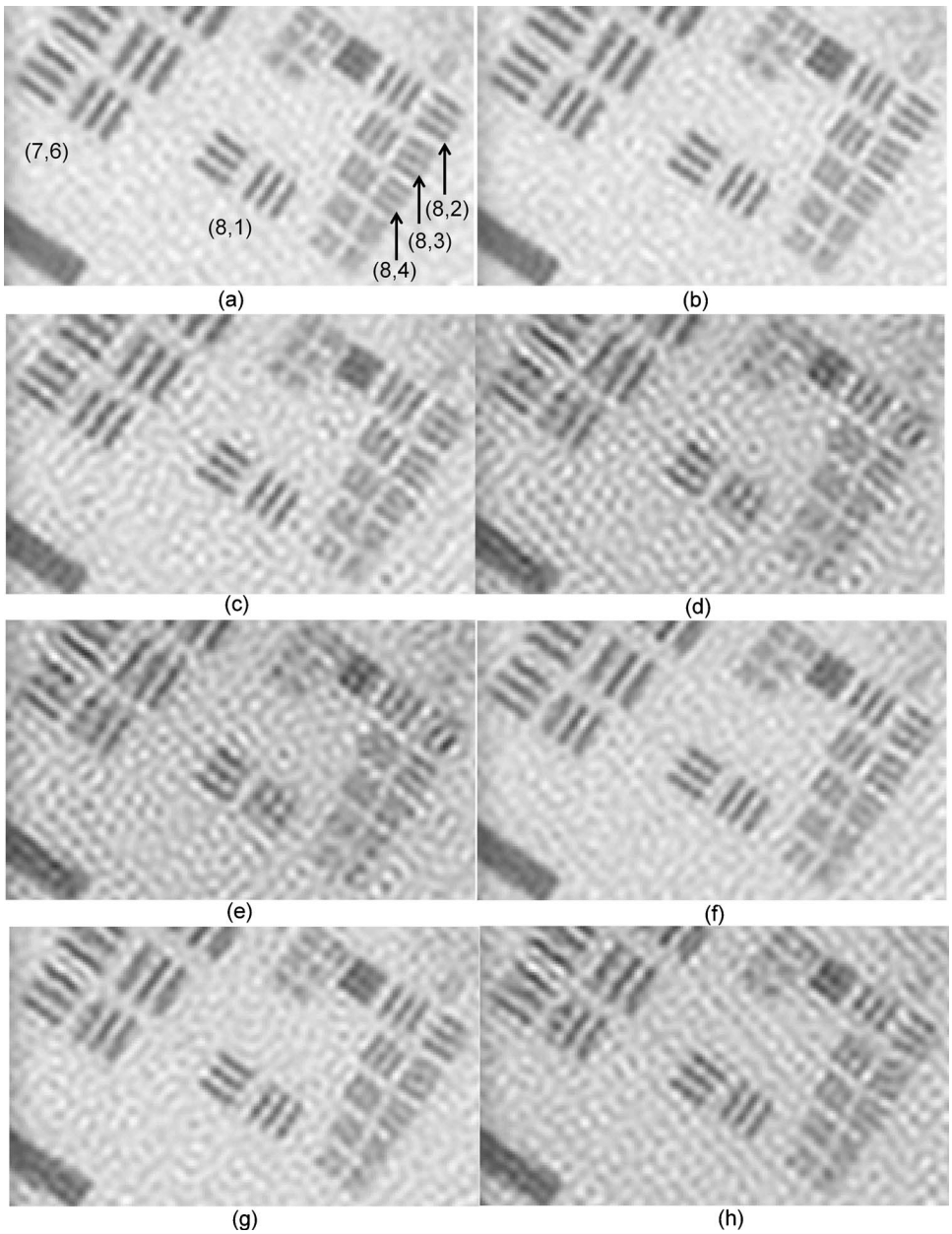


Fig. 5. (a)–(e) show the ~47% superresolved image obtained using two sets of (a) 20, (b) 12, (c) 6, (d) 4, (e) 3 sinusoidal grid patterned images in each orientation with random phase shifts in the sinusoidal illumination. (f)–(h) used two sets of (f) 6, (g) 4, and (h) 3 images with phase shifts well spaced over 360°.

residue in this orientation, but the residual peaks appear to be dim enough in magnitude as to not produce disturbing artifacts in the image.

Considering the size of the finest bars visible in this reconstruction (362 lp/mm) and the resolution of our conventional system (256 lp/mm), we can verify that the resolution in the reconstructed image is enhanced by at least 41%. We could not verify 47% superresolution as we would require bars having spacing close to 400 lp/mm in our object, whereas the next set of bars on the USAF bar target was 406 lp/mm which, at 49.6% superresolution, was outside the expected theoretical 47% superresolution.

### B. Minimizing Data Collection

The above superresolved reconstruction used two sets of 20 sinusoidal grid-patterned images in each set, with the sinusoidal illumination rotated by 90° in one set with respect to the other. This means that a total of 40 images went into the production of a single superresolved image. The effects of using sets of 12, 6, 4, and 3 images for each orientation of the sinusoidal illumination are shown in Figs. 5(b)–5(e) and their Fourier transforms in Figs. 6(b)–6(e), respectively. We again use a regularization constant of $c=0.1$ for all of these reconstructions.

The reconstruction that used $12\times2=24$ images in all, Fig. 5(b), still shows all the groups of bars up to group (8,4) of the USAF high-resolution bar target having a line spacing of 362 lp/mm (i.e., 2.8 $\mu$m), and has image quality comparable to Fig. 5(a). The reconstruction that used $6\times2=12$ images in all, Fig. 5(c), also shows that all the groups of bars up to group (8,4) of the USAF high-resolution bar target having a line spacing of 362 lp/mm

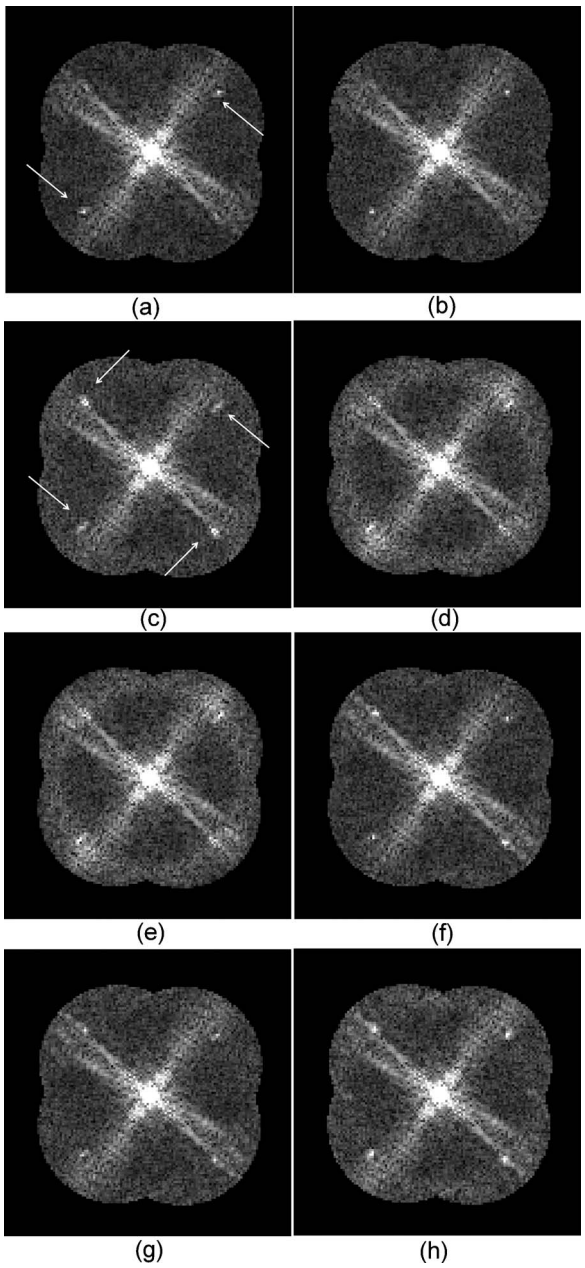


Fig. 6. (a)–(e) show the stretched Fourier transform of $a \sim 47\%$ superresolved image obtained using two sets of (a) 20, (b) 12, (c) 6, (d) 4, (e) 3 sinusoidal grid patterned images in each orientation with random phase shifts in the sinusoidal illumination. (f)–(h) used two sets of (f) 6, (g) 4, and (h) 3 images with phase shifts well spaced over 360°.

(i.e., 2.8 $\mu$m) are still discernible, although the colored noise in the image has significantly increased and the (8,4) group is barely discernible. The Fourier domain shows that residual peaks, labeled by white arrows, have increased compared to the case of using a larger number of images and now are visible for both orientations of the sinusoidal illumination. In the reconstruction that used $4 \times 2 = 8$ images in all, Fig. 5(d), the resolution appears to be only slightly better than the conventional reconstructed image. None of the bars beyond the conventionally visible (8,1) group are discernible here. The residual peaks in the Fourier domain are still distinctly visible and

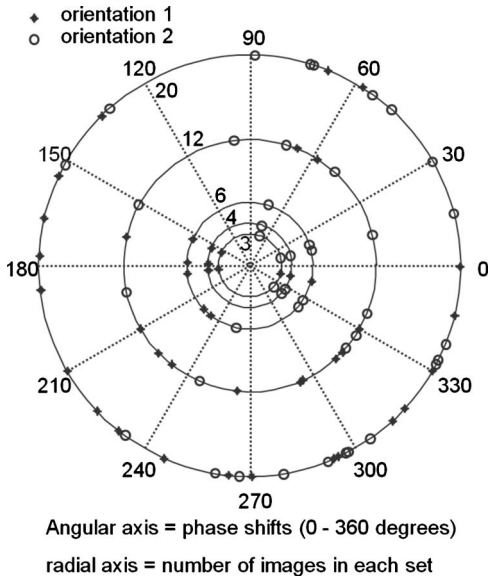


Fig. 7. Phase shift estimates for sinusoidally patterned images with random phase shifts having 20, 12, 6, 4, and 3 images in each set and 2 orientations for each set.

the SNR in the extended "superresolved" areas beyond the conventional OTF in the Fourier domain appears to be poor. The same holds for the case of the reconstruction that used $3 \times 2 = 6$ images in all, shown in Fig. 5(e) and its Fourier transform Fig. 6(e). No bars beyond the conventionally visible (8,1) group are visible and any resolution enhancement is indistinct.

Thus, although technically the minimum required number of images for each orientation is 3, in practice the number needed for useful superresolution depends on several factors. It primarily depends on the SNR of the conventional imaging system. Low SNR and low light levels require a greater number of images. Similarly greater amounts of superresolution, for which the OTF factor will be low, will lower the SNR for the superresolved spatial frequencies, requiring a greater number of images. If we had used a lower-spatial-frequency grid pattern, say, at 25% of the cutoff frequency, we would expect less superresolution (i.e., 25%). In this case the contrast of the sinusoidal pattern would be higher and hence the SNR in the grid patterned image would also be higher, and one would need fewer images for the 25% superresolution than needed to obtain close to 50%.

Further, as discussed in the SNR analysis section, the number of images required in each orientation for useful superresolution depends on the randomness of the phase shifts and, in this case, the motion of the object. If the images in each set have well-spaced phase shifts covering the entire 360° phase space, then fewer images will be needed to obtain discernible superresolution. If several images in a set have similar phase shifts, more images will be needed to add diversity. We plot the estimated phase shifts (along the angular axis) in our 20, 12, 6, 4, and 3 image sets (along the radial axis) for both orientations of the sinusoidal grid (plotted with asterisks and open circles) in Fig. 7. The plots show that the estimated phase shifts in the images for the case of sets of 6, 4, and 3 images are somewhat clumped in phase. We repeated

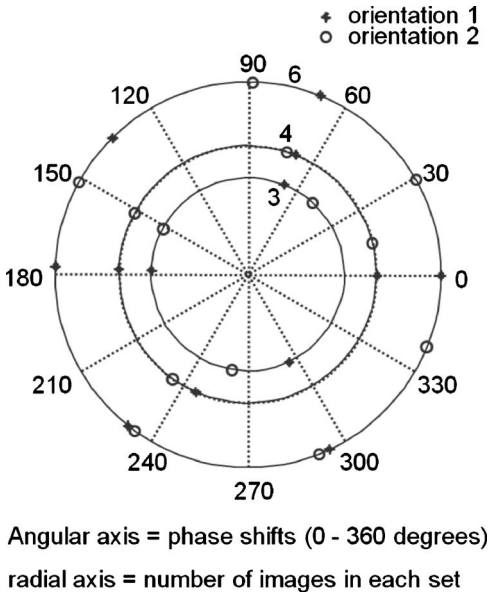


Fig. 8. Phase shift estimates for sinusoidally patterned images with phase shifts spread over 360° having 6, 4, and 3 images in each set and 2 orientations for each set.

the reconstruction for the case of 6, 4, and 3 image sets, with images that were chosen to have phase shifts somewhat better spaced in the 360° phase space (shown in Fig. 8). The reconstructed images are shown in Figs. 5(f)–(h) and the corresponding Fourier transforms are shown in Figs. 6(f)–6(h). We see a marked improvement in both the SNR and the effective visible resolution of the reconstructions. Here we can see that all the images show an improvement in resolution and all the bars up to group (8,4) of the USAF high-resolution bar target having a line spacing of 362 lp/mm (i.e., 2.8 $\mu$m) can now be resolved for the case of sets of 6, 4, as well as 3 images. Thus the diversity of phase shifts is very important in deciding the SNR of the superresolved reconstruction. For the case of random phase shifts one cannot guarantee well-spaced phase shifts, so it is prudent to take more than just three or four exposures with random phase shifts.

Thus the number of sinusoidally patterned images required to obtain a single superresolved image varies significantly depending on the imaging system, the illumination setup, and the application.

## 5. CONCLUSIONS

In this paper we have discussed a method to estimate the phase shifts in the sinusoidal illumination *a posteriori*, allowing us to apply the technique of structured illumination imaging to non-stationary objects such as *in vivo* tissue. We have verified the phase shift estimation technique experimentally. We estimated phase shifts in fluorescence microscopy images for a fluorescent USAF bar target having unknown, random translational motion and used them to obtain an artifact-free reconstruction having over 40% superresolution as expected. The object motion effectively introduces the required phase shifts in the sinusoidal illumination. The object in these images can be aligned to sub-pixel accuracy in post-processing by using a conventional image of the object as a reference. The phase of the sinusoidal illumination can be estimated *a posteriori* as demonstrated in this paper using a Fourier domain approach. This approach is more accurate for moderate spatial frequencies than for very high or very low spatial frequencies of the sinusoidal illumination. These phase-shift estimates may be further refined if used as initial estimates to iterative optimization-based algorithms if further accuracy in phase-shift estimation is desired. We assumed $\eta_i = 1$ in our reconstructions in this paper, but in the future we would like to estimate it from the distribution of phase values. We demonstrated the reconstruction of a superresolved image with negligible artifacts in the image when a reasonable number of images were used. The minimum number of images needed to obtain a single image with significant superresolution depends on the superresolution factor, the SNR, the randomness of the phase shifts, the contrast of the sinusoid, and the aberrations of the imaging and illumination systems. Greater amounts of superresolution, such as approaching 100%, would require a more customized illumination setup with a laser source producing higher contrast sinusoidal fringe illumination, three orientations of the sinusoidal illumination to cover the entire area of the extended OTF, and possibly a greater number of sinusoidally patterned images. The phase shift estimation algorithm should work on high-spatial-frequency sinusoidal illumination as long as it does not exceed about 90% of the diffraction limited cutoff or contain excessive noise.

Sinusoidally patterned illumination imaging can thus be applied to image objects having random and unknown translational motion to obtain superresolution. It would be advisable to take more than the minimum number of images for such randomly moving objects to ensure good SNR in the reconstruction. There is also some work pertaining to non-linear structured illumination [3,30], where the illumination excites a non-linear emission based on the saturated or stimulated emission of the fluorophore material producing spatial frequencies that are higher harmonics of the original sinusoidal illumination and lie beyond the illumination OTF. Such illumination could provide even greater amounts of superresolution. Our algorithms would have to be modified to adapt to such imaging techniques. Our approach and algorithms can also be used for axial optical sectioning in the presence of unknown phase shifts. We discuss this application in a future publication. This broadens the scope of its application to new areas such as *in vivo* imaging and imaging in vibration and motion-prone environments.

## APPENDIX A

This appendix contains derivations for the SNR analysis shown in Subsection 2.C.

First we consider four sinusoidally patterned images having phase shifts in the sinusoidal illumination, $2\varphi_n = 0$, $\pi/2$, $\pi$, and $3\pi/2$, and $\exp(\pm i 2\varphi_n) = 1$, $\pm i$, $-1$, and $\mp i$. Using Eq. (2) we obtain their four respective image Fourier transforms $\hat{\mathcal{G}}_1$, $\hat{\mathcal{G}}_2$, $\hat{\mathcal{G}}_3$, and $\hat{\mathcal{G}}_4$. The closed-form value for the noisy version of the conventional component image, $I_{c1}$, is given as

$$\hat{I}_{c1}(f_x,f_y) = \frac{1}{4}[\hat{\mathcal{G}}_1(f_x,f_y) + \hat{\mathcal{G}}_2(f_x,f_y) + \hat{\mathcal{G}}_3(f_x,f_y) + \hat{\mathcal{G}}_4(f_x,f_y)]$$
$$= \frac{1}{2}\mathcal{H}_1(0,0)\mathcal{H}_2(f_x,f_y)\mathcal{G}_o(f_x,f_y) + \frac{1}{4}[N_1(f_x,f_y) + N_2(f_x,f_y) + N_3(f_x,f_y) + N_4(f_x,f_y)]. \quad \text{(A1)}$$

The signal power spectrum in this image component is

$$\Phi_{S1}(f_x,f_y) = \left\langle \left| \frac{1}{2}\mathcal{H}_1(0,0)\mathcal{H}_2(f_x,f_y)\mathcal{G}_o(f_x,f_y) \right|^2 \right\rangle = \frac{1}{4}|\mathcal{H}_1(0,0)\mathcal{H}_2(f_x,f_y)|^2\Phi_o(f_x,f_y), \quad \text{(A2)}$$

where $\Phi_o = \langle|\mathcal{G}_o(f_x,f_y)|^2\rangle$ is the object power spectrum. The OTF for this image component is given by Eq. (7). The noise power spectrum is

$$\Phi_{N1}(f_x,f_y) = \frac{1}{16}[\sigma_{N1}^2 + \sigma_{N2}^2 + \sigma_{N3}^2 + \sigma_{N4}^2] = \frac{1}{4}\sigma^2, \quad \text{(A3)}$$

where $\sigma^2_{Nk}$ is the noise variance in each image, $k = 1,2,\ldots 4$. Here we assume that the four images contain statistically independent noise realizations having identical variances, $\sigma^2$. Using Eqs. (A2) and (A3) the power SNR for this image component is

$$SNR_{c1} = \frac{\Phi_{S1}(f_x,f_y)}{\Phi_{N1}} = \frac{1}{\sigma^2}|\mathcal{H}_1(0,0)\mathcal{H}_2(f_x,f_y)|^2\Phi_o(f_x,f_y). \quad \text{(A4)}$$

The noisy version of the superresolution component $I_{c2}$ is

$$[\mathcal{G}_1(f_x,f_y) - \mathcal{G}_3(f_x,f_y)] - i[\mathcal{G}_2(f_x,f_y) - \mathcal{G}_4(f_x,f_y)] = m\mathcal{H}_1(2f_o,0)\mathcal{H}_2(f_x,f_y)\mathcal{G}_o(f_x - 2f_o,f_y) + [N_1(f_x,f_y) - N_3(f_x,f_y)] - i[N_2(f_x,f_y) - N_4(f_x,f_y)]. \quad \text{(A5)}$$

Sub-pixel shifting this term in frequency space (by multiplying by a linear phase in the Fourier domain) and dividing by 4 for averaging, we obtain

$$\hat{I}_{c2}(f_x,f_y) = \frac{1}{4}m\mathcal{H}_1(2f_o,0)\mathcal{H}_2(f_x + 2f_o,f_y)\mathcal{G}_o(f_x,f_y) + \frac{1}{4}\{[N_1(f_x + 2f_o,f_y) - N_3(f_x + 2f_o,f_y)] - i[N_2(f_x + 2f_o,f_y) - N_4(f_x + 2f_o,f_y)]\}. \quad \text{(A6)}$$

The signal power spectrum for this component image is given by

$$\Phi_{S2}(f_x,f_y) = \left\langle \left| \frac{1}{4}m\mathcal{H}_1(2f_o,0)\mathcal{H}_2(f_x + 2f_o,f_y)\mathcal{G}_o(f_x,f_y) \right|^2 \right\rangle = \frac{1}{16}|m\mathcal{H}_1(2f_o,0)\mathcal{H}_2(f_x + 2f_o,f_y)|^2\Phi_o(f_x,f_y). \quad \text{(A7)}$$

The OTF affecting it is given by Eq. (10). The noise power spectrum for $\hat{I}_{c2}$ is

$$\Phi_{N2}(f_x,f_y) = \frac{1}{16}(\sigma_{N1}'^2 + \sigma_{N2}'^2 + \sigma_{N3}'^2 + \sigma_{N4}'^2) = \frac{1}{4}\sigma^2, \quad \text{(A8)}$$

where $\sigma_{Ni}'^2$ is the variance for the noise realizations shifted in frequency space to $(f_x - 2f_o,f_y)$. We again assume statistical independence and identical variances, $\sigma^2$, for the noise realizations. Therefore, the SNR for this image component is

$$SNR_{c2} = \frac{\Phi_{S2}(f_x,f_y)}{\Phi_{N2}} = \frac{1}{4\sigma^2}|m\mathcal{H}_1(2f_o,0)\mathcal{H}_2(f_x + 2f_o,f_y)|^2\Phi_o(f_x,f_y). \quad \text{(A9)}$$

The SNR for $\hat{I}_{c3}$ can be derived in a similar manner by replacing $i$ by $-i$ and $2f_o$ by $-2f_o$ in the above equation. Similarly we derive the closed form SNR for image components obtained for sinusoidally patterned images where $2\varphi_n = 0$, $\pi/4$, $\pi/2$, and $3\pi/4$, $\exp(\pm i2\varphi_n) = 1$, $(1 \pm i)/\sqrt{2}$, $\pm i$, and $(-1 \pm i)/\sqrt{2}$. The Fourier transforms of these images are given by $\hat{\mathcal{G}}_1$, $\hat{\mathcal{G}}_2$, $\hat{\mathcal{G}}_3$, and $\hat{\mathcal{G}}_4$. For this case, the noisy version of the first component can be obtained optimally in closed form as

$$\hat{I}_{c1}(f_x,f_y) = \left(\frac{1+\sqrt{2}}{2\sqrt{2}}\right)[\hat{\mathcal{G}}_1(f_x,f_y) + \hat{\mathcal{G}}_4(f_x,f_y)] - \frac{1}{2\sqrt{2}}[\hat{\mathcal{G}}_2(f_x,f_y) + \hat{\mathcal{G}}_3(f_x,f_y)]$$
$$= \frac{1}{2}\mathcal{H}_1(0,0)\mathcal{H}_2(f_x,f_y)\mathcal{G}_o(f_x,f_y) + \left(\frac{1+\sqrt{2}}{2\sqrt{2}}\right)[N_1(f_x,f_y) + N_4(f_x,f_y)] - \frac{1}{2\sqrt{2}}[N_2(f_x,f_y) + N_3(f_x,f_y)]. \quad \text{(A10)}$$

The signal power spectrum in this component is

$$\Phi_{S1}(f_x,f_y) = \left\langle \left| \frac{1}{2}\mathcal{H}_1(0,0)\mathcal{H}_2(f_x,f_y)\mathcal{G}_o(f_x,f_y) \right|^2 \right\rangle = \frac{1}{4}|\mathcal{H}_1(0,0)\mathcal{H}_2(f_x,f_y)|^2\Phi_o(f_x,f_y). \quad \text{(A11)}$$

The noise power spectrum is

$$\Phi_{N1}(f_x,f_y) = \left(\frac{1+\sqrt{2}}{2\sqrt{2}}\right)^2(\sigma_{N1}^2 + \sigma_{N4}^2) + \left(\frac{1}{2\sqrt{2}}\right)^2(\sigma_{N2}^2 + \sigma_{N3}^2) = \frac{\sqrt{2}+1}{\sqrt{2}}\sigma^2 = 1.7\sigma^2, \quad \text{(A12)}$$

where, as before, $\sigma_{Nk}{}^2$ is the noise variance in the image, $k = 1,2,\ldots 4$, and we assume statistically independent noise realizations in the four images with identical variances, $\sigma^2$. Therefore the power SNR for this image component is

$$SNR_{c1} = \frac{\Phi_{S1}(f_x,f_y)}{\Phi_{N1}} = \frac{1}{6.8\sigma^2}|\mathcal{H}_1(0,0)\mathcal{H}_2(f_x,f_y)|^2\Phi_o(f_x,f_y), \tag{A13}$$

which is 6.8 times less than for the case of equally spaced phase shifts given by Eq. (A4).

The noisy version of the superresolution component $I_{c2}$ for the present case can be optimally computed as

$$\begin{aligned}&(0.04+i0.5)\hat{\mathcal{G}}_1(f_x,f_y)+(0.3-i0.4)\hat{\mathcal{G}}_2(f_x,f_y)\\&\quad+(0.1-i0.5)\hat{\mathcal{G}}_3(f_x,f_y)+(-0.4+i0.3)\hat{\mathcal{G}}_4(f_x,f_y)\\&=\frac{1}{4}m\mathcal{H}_1(2f_o,0)\mathcal{H}_2(f_x,f_y)\mathcal{G}_o(f_x-2f_o,f_y)\\&\quad+(0.04+i0.5)N_1(f_x,f_y)+(0.3-i0.4)N_2(f_x,f_y)\\&\quad+(0.1-i0.5)N_3(f_x,f_y)+(-0.4+i0.3)N_4(f_x,f_y).\end{aligned} \tag{A14}$$

As before, sub-pixel shifting this term in frequency space (by multiplying by a linear phase in the Fourier domain), we obtain

$$\begin{aligned}\hat{I}_{c2}(f_x,f_y) &= \frac{1}{4}m\mathcal{H}_1(2f_o,0)\mathcal{H}_2(f_x+2f_o,f_y)\mathcal{G}_o(f_x,f_y)\\&\quad+(0.04+i0.5)N_1(f_x+2f_o,f_y)\\&\quad+(0.3-i0.4)N_2(f_x+2f_o,f_y)\\&\quad+(0.1-i0.5)N_3(f_x+2f_o,f_y)\\&\quad+(-0.4+i0.3)N_4(f_x+2f_o,f_y).\end{aligned} \tag{A15}$$

The signal power spectrum for this image component is

$$\begin{aligned}\Phi_{S2}(f_x,f_y) &= \left\langle\left|\frac{1}{4}m\mathcal{H}_1(2f_o,0)\mathcal{H}_2(f_x+2f_o,f_y)\mathcal{G}_o(f_x,f_y)\right|^2\right\rangle\\&=\frac{1}{16}|m\mathcal{H}_1(2f_o,0)\mathcal{H}_2(f_x+2f_o,f_y)|^2\Phi_o(f_x,f_y).\end{aligned} \tag{A16}$$

Its noise power spectrum is

$$\begin{aligned}\Phi_{N2}(f_x,f_y) &= (0.04+i0.5)^2\sigma_{N1}'^2+(0.3-i0.4)^2\sigma_{N2}'^2\\&\quad+(0.1-i0.5)^2\sigma_{N3}'^2+(-0.4+i0.3)^2\sigma_{N4}'^2=0.98\sigma^2,\end{aligned} \tag{A17}$$

where $\sigma_{Ni}'^2$ and $\sigma^2$ are as defined before. Its power SNR is given as

$$\begin{aligned}SNR_{c2} &= \frac{\Phi_{S2}(f_x,f_y)}{\Phi_{N2}}\\&=\frac{1}{15.7\sigma^2}|m\mathcal{H}_1(2f_o,0)\mathcal{H}_2(f_x+2f_o,f_y)|^2\Phi_o(f_x,f_y).\end{aligned} \tag{A18}$$

which is 3.9 times less than for the case of equally spaced phase shifts given by Eq. (A9).

## REFERENCES


1. M. Gustaffson, "Surpassing the lateral resolution limit by a factor of two using structured illumination microscopy," J. Microsc. **198**, 82–87 (2000).
2. M. Gustafsson, "Extended-resolution reconstruction of structured illumination microscopy data," in *Computational Optical Sensing and Imaging Topical Meetings* on CD-ROM, Technical Digest (Optical Society of America, 2005), paper JMA2.
3. M. Gustafsson, L. Shao, D. A. Agard, and J. W. Sedat, "Fluorescence microscopy without resolution limit," in *Biophotonics/Optical Interconnects and VLSI Photonics/WBM Microcavities*, 2004 Digest of the LEOS Summer Topical Meetings (IEEE, 2004), Vol.2, pp. 28–30.
4. R. Heintzmann and C. Cremer, "Laterally modulated excitation microscopy: Improvement of resolution by using a diffraction grating," Proc. SPIE **3568**, 185–196 (1999).
5. M. Gustafsson, "Extended resolution fluorescence microscopy," Curr. Opin. Struct. Biol. **9**, 627–634 (1999).
6. W. Lukosz, "Optical systems with resolving powers exceeding the classical limits II," J. Opt. Soc. Am. **57**, 932–941 (1967).
7. D. Mendlovic, A. W. Lohmann, N. Konforti, I. Kiryuschev, and Z. Zalevsky, "One-dimensional superresolution optical system for temporally restricted objects," Appl. Opt. **36**, 2353–2359 (1997).
8. E. Sabo, Z. Zalevsky, D. Mendlovic, N. Konforti, and I. Kiryuschev, "Superresolution optical system using three fixed generalized gratings: experimental results," J. Opt. Soc. Am. A **18**, 514–520 (2001).
9. A. Shemer, Z. Zalevsky, D. Mendlovic, N. Konforti, and E. Marom, "Time multiplexing superresolution based on interference grating projection," Appl. Opt. **41**, 7397–7404 (2002).
10. S. W. Hell and J. Wichmann, "Breaking the diffraction resolution limit by stimulated emission: stimulated-emission-depletion fluorescence microscopy," Opt. Lett. **19**, 780–782(1994).
11. X. Chen and S. R. J. Brueck, "Imaging interferometric lithography: approaching the resolution limits of optics," Opt. Lett. **24**, 124–126 (1999).
12. C. J. Schwarz, Y. Kuznetsova, and S. R. J. Brueck, "Imaging interferometric microscopy," Opt. Lett. **28**, 1424–1426 (2003).
13. V. Mico, Z. Zalevsky, and J. García, "Superresolution optical system by common-path interferometry," Opt. Express **14**, 5168–5177 (2006).
14. G. E. Cragg and P. T. C. So, "Lateral resolution enhancement with standing evanescent waves," Opt. Lett. **25**, 46–48 (2000).
15. E. Chung, D. Kim, and P. T. So, "Extended resolution wide-field optical imaging: objective-launched standing-wave total internal reflection fluorescence microscopy," Opt. Lett. **31**, 945–947 (2006).
16. T. Wilson and C. J. R. Sheppard, *Theory and Practice of Scanning Optical Microscopy* (Academic, 1983).
17. S. A. Shroff, J. R. Fienup, and D. R. Williams, "Phase-shift estimation in sinusoidally illuminated images for lateral superresolution," J. Opt. Soc. Am. A **26**, 413–424 (2009).
18. S. A. Shroff, J. R. Fienup, and D. R. Williams, "OTF compensation in structured illumination superresolution images," Proc. SPIE **7094**, 709402-1–11 (2008).
19. S. A. Shroff, J. R. Fienup, and D. R. Williams, "Phase shift estimation in structured illumination imaging for lateral resolution enhancement," in *Signal Recovery and Synthesis*, Topical Meetings on CD-ROM, OSA Technical Digest (CD) (Optical Society of America, 2007), paper SMA2.
20. S. A. Shroff, J. R. Fienup, and D. R. Williams, "Estimation of phase shifts in structured illumination for high resolution imaging," in *Frontiers in Optics*, OSA Technical Digest (CD) (Optical Society of America, 2007), paper FMH4.
21. G. Strang, *Linear Algebra and Its Applications* (Thomson Learning, Inc., 1998).
22. L. P. Yaroslavsky and H. J. Caulfield, "Deconvolution of

multiple images of the same object," Appl. Opt. **33**, 2157–2162 (1994).
23. C. W. Helstrom, "Image restoration by the method of least squares," J. Opt. Soc. Am. **57**, 297–303 (1967).
24. D. J. Tolhurst, Y. Tadmore, and T. Chao, "Amplitude spectra of natural images," Ophthalmic Physiol. Opt. **12**, 229–232 (1992).
25. A. van der Schaaf and J. H. van Hateren, "Modelling the power spectra of natural images: statistics and information," Vision Res. **36**, 2759–2770 (1996).
26. D. R. Gerwe, M. Jain, B. Calef, and C. Luna, "Regularization for nonlinear image restoration using a prior on the object power spectrum," in Proc. SPIE **5896**, 1–15 (2005).
27. S. T. Thurman and J. R. Fienup, "Wiener reconstruction of undersampled imagery," J. Opt. Soc. Am. A **26**, 283–288 (2009).
28. L. H. Schaefer, D. Schuster, and J. Schaffer, "Structured illumination microscopy: artefact analysis and reduction utilizing a parameter optimization approach," J. Microsc. **216**, 165–174 (2004).
29. M. Guizar-Sicairos, S. T. Thurman, and J. R. Fienup, "Efficient subpixel image registration algorithms," Opt. Lett. **33**, 156–158 (2008).
30. R. Heintzmann, T. M. Jovin, and C. Cremer, "Saturated patterned excitation microscopy—a concept for optical resolution improvement," J. Opt. Soc. Am. A **19**, 1599–1609 (2002).